HHS Public Access

Author manuscript

J Struct Biol. Author manuscript; available in PMC 2021 April 01.

Published in final edited form as:

J Struct Biol. 2020 April 01; 210(1): 107474. doi:10.1016/j.jsb.2020.107474.

DIRECT COMPARISON OF OPTICAL AND ELECTRON MICROSCOPY METHODS FOR STRUCTURAL CHARACTERIZATION OF EXTRACELLULAR VESICLES

Jade M. Noble[a,1], **LaDeidra Monét Roberts**[b,1], **Netta Vidavsky**[c,1], **Aaron E. Chiou**[b], **Claudia Fischbach**[b], **Matthew J. Paszek**[a,e], **Lara A. Estroff**[c,e], **Lena F. Kourkoutis**[d,e]

[a]Robert Frederick Smith School of Chemical and Biomolecular Engineering, Cornell University, Ithaca, New York, USA.

[b]Nancy E. and Peter C. Meinig School of Biomedical Engineering, Cornell University, Ithaca, New York, USA.

[c]Department of Materials Science and Engineering, Cornell University, Ithaca, New York, USA.

[d]School of Applied and Engineering Physics, Cornell University, Ithaca, New York, USA.

[e]Kavli Institute at Cornell for Nanoscale Science, Cornell University, Ithaca, New York, USA.

Abstract

As interest in the role of extracellular vesicles in cell-to-cell communication has increased, so has the use of microscopy and analytical techniques to assess their formation, release, and morphology. In this study, we evaluate scanning electron microscopy (SEM) and cryo-SEM for characterizing the formation and shedding of vesicles from human breast cell lines, parental and hyaluronan synthase 3-(HAS3)-overexpressing MCF10A cells grown directly on transmission electron microscopy (TEM) grids. While cells imaged with conventional- and cryo-SEM exhibit distinct morphologies due to the sample preparation process for each technique, tubular structures protruding from the cell surfaces were observed with both approaches. For HAS3-MCF10A cells, vesicles were present along the length of membrane protrusions. Once completely shed from the cells, extracellular vesicles were characterized using nanoparticle tracking analysis (NTA) and cryo-TEM. The size distributions obtained by each technique were different not only in the range of vesicles analyzed, but also in the relative proportion of smaller-to-larger vesicles. These differences are attributed to the presence of biological debris in the media, which is difficult to differentiate from vesicles in NTA. Furthermore, we demonstrate that cryo-TEM can be used to distinguish between vesicles based on their respective surface structures, thereby providing a path

*Corresponding: lena.f.kourkoutis@cornell.edu, lae37@cornell.edu, paszek@cornell.edu, Phone number: 607-255-9121, Fax: 607-255-7658.

1.Authors contributed equally to this work.

Author Contributions

J.M.N., **L.M.R.**, **N.V.**: Methodology, Investigation, Writing - Original Draft; **A.E.C.**: Methodology, Investigation; **C.F.**: Supervision, Writing - Review & Editing; **M.J.P.**: Conceptualization, Supervision, Writing - Review & Editing; **L.A.E., L.F.K.**: Conceptualization, Methodology, Supervision, Writing - Original Draft & Review & Editing

to differentiating vesicle subpopulations and identifying their size distributions. Our study emphasizes the necessity of pairing several techniques to characterize extracellular vesicles.

Keywords

Cryo-scanning electron microscopy; cryo-transmission electron microscopy; nanoparticle tracking analysis; microvesicles; exosomes; extracellular vesicles; cellular communication; glycocalyx; breast cancer

Introduction

Recent literature has demonstrated that cells release a variety of membrane-bound structures into the extracellular environment known as extracellular vesicles (EVs). These structures have been shown to play a key role in long and short range cell-to-cell communication by delivering specific cargos to other cells or the extracellular space (Antonyak et al., 2011; Yuana et al., 2013). Two subtypes of EVs are exosomes and microvesicles (MVs), which are currently differentiated by their size and mode of biogenesis. Whether or not morphological characteristics may be used to differentiate both subtypes, however, remains unclear due in part to a lack of high resolution techniques that allow comparing exosomes and MVs in their native state. The current understanding is that exosomes are secreted via exocytosis from endosomal multivesicular bodies (MVB) and are typically ~50-100 nm in diameter. Microvesicles, on the other hand, are directly shed from the plasma membrane (Muralidharan-Chari et al., 2010) and are comparatively larger (~200 nm-1 μm). EVs are known to be released by cells under physiological conditions, such as embryogenesis, reproduction (Desrochers et al., 2016; Tannetta et al., 2014) and muscle regeneration (Nakamura et al., 2015), as well as pathological conditions, such as thrombosis and tumor metastasis (Becker et al., 2016; Furie and Furie, 2004; György et al., 2011; Le et al., 2014; van der Pol et al., 2012). Despite their prevalence in the body and involvement in multiple biological processes, the size and morphology of these vesicles are relatively unknown.

Understanding the function of EVs requires methods that successfully isolate and detect them, preferably without disturbing the vesicles' native morphology. The formation of EVs is associated with structural modifications in the cell's plasma membrane, a nanoscale phenomenon best assessed with high-resolution imaging methodologies (van Niel et al., 2018). Techniques such as scanning electron microscopy (SEM) provide such resolving power and are routinely used for cell imaging. Biological samples prepared for conventional SEM are, however, chemically fixed and dehydrated, which often introduces artefacts. For soft matter materials with high water content, a viable alternative to room temperature SEM is cryo-SEM. In this technique, first demonstrated in the early 1970s (Echlin et al., 1970, Echlin, 1971), samples are preserved in a near-native state through rapid freezing and imaged under cryogenic conditions. In 1981, vitrification to prepare hydrated samples for direct investigation by cryo-TEM was introduced (Dubochet and McDowall, 1981). Historically used extensively to understand tissue structure and physiology of plants and model organisms (Utsumi et al., 1998, Charuvi et al., 2016; Cochard et al.,2000; McCully et

al., 2009; Mahamid et al., 2010), cryo-SEM has been recently adopted to examine cancer cell morphology and EV shedding (Koifman et al., 2017).

EV size, concentration, and composition are often analyzed with various techniques (Colombo et al., 2014, Szatanek et al., 2017). In particular, nanoparticle tracking analysis (NTA) calculates EV particle size by measuring the diffusion constants of suspended particles in Brownian motion and solving the Stokes-Einstein equation to determine their hydrodynamic diameters (Soo et al., 2012). Transmission electron microscopy (TEM), in comparison, allows for characterization of both the size and morphology of individual vesicles. For instance, a range of morphologies have been reported for MVs (Issman et al., 2013), including “cup-shaped” vesicles observed using conventional TEM (van Niel et al., 2018). Enhanced confidence in the presence and morphology of MVs has been achieved with the preservation of EVs in a near-native state using vitrification (van Niel et al., 2018). Cryo-TEM is, therefore, more often used now for analyzing EVs. Both NTA and cryo-TEM analysis of EVs involve harvesting vesicles from cell cultures and purification before analysis. The methods used for EV isolation and sample preparation may, however, additionally impact which EV subtypes are ultimately collected for analysis as well as their observed morphologies (Issman et al., 2013). Therefore, comparison of these analytical techniques is necessary for a holistic approach to explore EV-related phenomena.

In this study we compared conventional and cryo-SEM in characterizing cell morphology and EV release. Additionally, we used NTA and cryo-TEM to characterize isolated EVs and evaluated the comparative strengths and disadvantages of each technique. We use the MCF10A cell line (Soule et al., 1990), a non-tumorigenic, human mammary epithelial cell line as a control, and hyaluronic acid synthase-3 (HAS3)-overexpressing MCF10A cells (HAS3-10A) where overexpression of HAS3 has been previously shown to produce intermediate to long forms of hyaluronic acid (HA) and EV production is increased (Koistinen et al., 2015; Rilla et al., 2013; Shurer et al., 2019). Given that increased EV production by mammary epithelial cells is associated with tumor progression and because EVs themselves can transform non-malignant cells (Antonyak et al., 2011), the utilized cell lines represent appropriate model systems to study the potential connection of our findings to breast cancer development and progression.

Materials and Methods

Cell lines and culture

MCF10A and MDA-MB231 cells were obtained from ATCC (Manassas, VA). MDA-MB231 were cultured in complete DMEM medium while MCF10A cells were cultured in DMEM/F12 basal media supplemented with 5% horse serum, 20 ng/mL EGF, 10 μg/mL insulin, 500 ng/mL hydrocortisone, 100 ng/mL cholera toxin, and penicillin/streptomycin. Modified MCF10A cells were produced through lentiviral transfection of a tetracycline-inducible vector as described previously (Shurer et al., 2014; Shurer et al., 2019). Modified MCF10A cells were produced through lentiviral transfection with a pLV TetOn HAS3 vector (Shurer et al., 2019). All cell lines were maintained at 37°C and 5% CO_2.

Cell culture on TEM grids

All grid handling was carried out inside glass-bottom dishes (MatTek, 35-mm dish diameter, 20 mm glass) under sterile conditions. Quantifoil R1/4 holey carbon 200 mesh gold TEM grids (Quantifoil Micro Tools, Jena, Germany) were glow discharged for 10 seconds to improve hydrophilicity. Grids were then sterilized in 70% ethanol and washed with DI water three times. To enhance cell adhesion to the carbon film TEM grids were functionalized with fibronectin. For fibronectin coating, grids were incubated with 30 μg/mL human fibronectin reconstituted in DI water, 37°C, for 2 hours. After coating, grids were washed with DI water three times, followed by washing with culture media and incubation in culture media for 1 hour. MDA-MB231 cells were used initially to establish protocols for cell seeding and subsequent handling. All other experiments were performed with HAS3 cells and control cells plated at a density of 150,000 cells/mL of media with 2 mL applied to each dish. Cells were induced with 1 μg/mL doxycycline for 48 hours. A representation of the experimental setup is shown in Fig. 1.

Fluorescence labeling and imaging

Grids were washed twice with PBS buffer and fixed with 10% formalin at room temperature for 20 minutes. The formalin was removed, and grids were washed three times for 2 minutes each with PBSX (0.05% TritonX in PBS). Fluorescence staining solutions of DAPI (1:5000) and Phalloidin Alexa Fluor 488 (1:200) in 1% BSA/PBS were prepared and kept covered with aluminum foil. Grids were immersed and incubated in the fluorescence staining solutions at room temperature for 1 hour, followed by two washes with PBS. Grids were imaged under PBS using a Zeiss LSM 710 Confocal Microscope with 40x water immersion objective, and 405 nm (DAPI) and 488 nm (Alexa Fluor 488) lasers with pinhole of 36.2 μm and emission wavelengths of 452.5 nm and 562.5 nm. Z stacks were acquired with 0.46 μm intervals and were processed using ImageJ.

SEM imaging

Cells were fixed on TEM grids using freshly prepared Trump's fixative (4 mL 10x PBS, 10 mL 16% paraformaldehyde, 4 mL 10% glutaraldehyde, 22 mL ddH_2O). First, grids were rinsed with Trump's fixative at 37°C, which was removed immediately. Fresh Trump's fixative was added at 37°C and grids were stored at 4°C overnight before removal. Grids were then immersed in 1% osmium tetroxide in 0.05 M cacodylate buffer on ice for 40 minutes. Cacodylate buffer was added in excess for 10 minutes and removed. Fresh buffer was added for another 10 minutes. This process was repeated twice. Grids were washed with 25% and 50% EtOH on ice for 10 minutes, followed by 70% EtOH overnight. Grids were washed with 95%, 100%, 100% EtOH on ice for 10 minutes each before undergoing critical point drying (CPD). Samples were coated with Au-Pd (at 10 mA for 15 seconds) and imaged in a Mira3 FESEM (Tescan, Czech Republic). High-resolution images were acquired at 5 keV and a 3 mm working distance with the in-beam secondary electron detector. Brightness and contrast were adjusted using Adobe Photoshop to optimize visibility of cellular features. Image processing was done consistently across all conditions and regions. The vesicle size distribution shown in Fig. 3F was determined directly from the SEM image

by estimating each vesicle as an ellipse and calculating the average of the minor and major axes.

Extracellular vesicle isolation

All cell lines were grown to high confluency at 10,000 cells/cm^2 in T-150 flasks for 42 hours and induced as described above. Media was collected from cells and spun at 200 × *g* for 5 minutes to pellet any detached cells from doxycycline induction. Adhered cells were rinsed with PBS twice before being combined with detached cells and serum starved with 3 mL of serum free-media for 6 hours to avoid contamination from nascent exosomes from serum. Following serum starvation, media was harvested and clarified by centrifugation at 600 × *g* for 5 minutes, then 2 mL of media was collected and spun at 600 × *g* for 5 minutes. 1.5 mL of media was collected as the final volume for experiments. Cells were detached and combined with any detached cells due to doxycycline induction and counted to obtain the concentration of cells for calculating the extracellular vesicle production rate (vesicles/cell/6 hours).

Nanoparticle Tracking Analysis (NTA)

To quantify extracellular vesicles released from the cells, clarified harvested media was analyzed using the Nanosight NS300 nanoparticle tracking analysis instrument (Malvern). Imaging was performed for 60 s with 5 captures per sample. Particles were analyzed using Malvern Nanoparticle Tracking Analysis Software. Following particle tracking captures, samples were recovered from the device post-NTA for correlative analysis by cryo-TEM. To ensure that NTA sample flow through the device did not influence our cryo-TEM data, we compared post-NTA samples to those that were not analyzed by NTA and found no difference in the sample size.

Plunge-freezing vitrification

For analysis of cells cultured on grids, grids were lifted out of cell culture dishes, blotted from the reverse side and immediately plunged into a liquid ethane/propane mixture cooled to liquid nitrogen temperature using a custom-built vitrification apparatus (MPI, Martinsried, Germany). For analysis of isolated extracellular vesicles post-NTA, 3-5 μL of harvested media were pipetted onto holey carbon 200 mesh copper grids (Quantifoil Micro Tools, Jena, Germany) with hole sizes of ~2 μm. The grids were blotted from the reverse side and immediately plunge-frozen as described above. The plunge-frozen grids were stored in sealed cryo-boxes in liquid nitrogen until used.

Cryo-SEM

Cryo-immobilized cells on TEM grids were imaged in a FEI Strata 400S DualBeam FIB/SEM system equipped with a Quorum PP3010T cryo-FIB/SEM system that enables cryogenic experiments. First, grids were heated in the preparation chamber from −150°C to −100°C for 20 minutes and then −90°C for 1 minute to allow for ice sublimation and to expose the cell surfaces. Sublimation times were optimized by sequentially heating the sample, transferring it into the main microscope and imaging the surface by cryo-SEM. Grids were then sputter coated with Au-Pd at 10 mA for 10 seconds in the Quorum

preparation chamber with the sample cooled to - 150°C. Note that coating of the sample to minimize charging effects can be avoided when operating at low voltage near the charge neutrality point (Goldstein et al., 2018, Joy and Joy, 1995). High-resolution images were acquired at −165°C, 3 keV and 68 pA and a working distance of 7 mm with a secondary electron Everhart-Thornley Detector (ETD). SEM imaging using secondary electrons provides direct information about the cell surface topography (Goldstein et al., 2018). Brightness and contrast were adjusted using Adobe Photoshop to optimize visibility of cellular features. Image processing was done consistently across all conditions and regions.

Cryo-TEM

Cryo-TEM was performed on a Titan Themis (Thermo Fisher Scientific, Waltham, MA) operated at 300 kV in energy-filtered mode equipped with a high brightness field-emission gun (XFEG), and a 3838x3710 pixel Gatan K2 Summit direct detector camera (Gatan, Pleasanton, CA) operating in counted, dose-fractionated mode. Images were collected at defoci between −1 and −3 μm. Images were binned by 2, resulting in pixel sizes of 0.51-1.09 nm. Vesicles sizes were measured using ImageJ software. Because the vesicles were approximately spherical, the average diameter was determined by taking the average of the vesicles' widths and lengths. For identification of subpopulations, vesicles smaller than ~120 nm were inspected at high magnification and classified either as microvesicles or exosomes based on the presence (microvesicles) or absence (exosomes) of surface structure. Vesicles larger than 120 nm were designated as microvesicles. High magnification imaging of a subset of these larger vesicles confirmed the presence of surface structure.

Results and Discussion

For reliable characterization and quantification, it is important to consider that during any step in the sample preparation, cells may undergo non-physiological structural modifications. To remove intermediate sample processing steps, HAS3 and control cells were cultured directly onto fibronectin-coated gold TEM grids for 48 hours. Cells grew uniformly in areas coated with fibronectin, both on and off the grid (Fig. 1). To assess whether the morphology of the cells was altered following culture on TEM grids, we stained for filamentous actin (F-actin). We found that cells cultured on grids were similar to cells cultured on traditional substrates, such as glass or polystyrene as confirmed through fluorescent microscopy (Fig. 1C).

When examined with conventional SEM, the surfaces of chemically-fixed cells appeared relatively flat with tubular extensions protruding from the cell surfaces of both HAS3 and control cells (Fig. 2A, C). The same cell types observed with cryo-SEM, however, appeared rounder in the out-of-plane direction, with fewer obvious protrusions (Fig. 2B, D; Fig. S1). Tubular extensions were present in the cryo-SEM images, however, these extensions on the cell surface laid flat against the grid. These extensions were present in cells imaged with both conventional and cryo-SEM and cannot be a fixation artefact (Fig. 2D; Fig. S1). The roundedness or flatness of cells cannot be attributed to variation in cell adhesion, as cells for SEM and cryo-SEM were grown under the same conditions. Indeed, there is no significant difference in the average cell axis length between SEM and cryo-SEM (Table S1). Instead,

we hypothesize that the morphological differences in cells observed with conventional and cryo-SEM are both the consequences of the sample preparation process for each technique. Although control cells also have tubular extensions, they were both shorter and less numerous (Fig. 2A) than the extensions seen in HAS3 cells (Fig. 2C). These tubular structures and the mechanism of their extension was investigated in detail in our recent work (Shurer et al., 2019) and independently verified in MCF10A cells expressing other glycopolymers (Mockl et al., 2019).

In conventional SEM, cells are dehydrated during the chemical fixation process, and the lack of water content may cause cells to appear flatter than if they were preserved in a liquid-hydrated state. On the other hand, blotting samples before plunge freezing for cryo-SEM likely affected the extensions on the cell surface, causing them to lie flat on the grid (Fig. 2B, D; Fig. S1). This appearance is different than the erect extensions on cells prepared for conventional SEM (Fig 2A, C). Consequently, choosing the appropriate technique depends on the cellular features of interest and their location in the cell. Protruding structures, such as cell tubular extensions, filopodia, or microvilli, can be imaged on the cell surface by conventional SEM. Chemical fixation, dehydration, and coating, however, might alter the morphologies of these structures. On the other hand, blotting in preparation for plunge-freezing can cause deformation of extended structures protruding from the cell surface. We have demonstrated that conventional and cryo-SEM can both be used to image the cellular surface, with each technique having its respective strengths and limitations. Rather than choosing one technique or the other, a more reasonable approach is to use both techniques and leverage the strengths of each approach.

We further assessed these techniques to directly validate the presence of MVs prior to shedding from the plasma membrane. Spherical features consistent with previous studies (Shurer et al., 2019) were observed on the surfaces of HAS3 cells as compared to control cells, which were not found to possess MVs on their tubular extensions (Fig. 3A; Fig. 2A). Although dimensionally consistent with MVs (Fig. 3B, C, F), further investigation of these structures with high-resolution imaging techniques are necessary for a positive identification and validation.

For direct comparison with existing work on these cell lines, we have also imaged HAS3 and MCF10A control cells grown on TEM grids using confocal fluorescence microscopy. HAS3 cells showed a high intensity of actin expression when compared to the control (Fig. 3D, E). The higher intensities in HAS3 cells are attributed to an increased density of actin microfilaments contained within tubular extensions protruding from the cell surface (Fig. 2B,C; 3D,E) (Shurer et al., 2019). These structures are thin and finger-like, and no wider than 100-200 nm in diameter (Fig. 3B-C).

Comparison of cryo-TEM and NTA in extracellular vesicle expression and diameter distributions

Results from both conventional and cryo-SEM and fluorescence microscopy provided insight into the surface morphology of cells, revealing both membrane protrusions and microvesicles around the cellular membrane. The majority of studies, however, examines exosome secretion and microvesicle release from the plasma membrane in post-isolation

vesicles. While isolated vesicles can be imaged relatively easily in an electron microscope, SEM does not provide the resolution to distinguish microscopic structural features on the surface of vesicles. A technique that can resolve the native surface structure could help identify microvesicles from other vesicles and therefore fill an unmet need since microvesicles currently do not possess any markers for detection. Cryo-TEM has the potential to fill this gap as it offers high spatial resolution and the ability to image EVs preserved in a near-native state using vitrification, thereby improving confidence in the presence and morphology of MVs compared to traditional approaches using chemical fixation (van Niel et al., 2018). Here, EVs isolated from cells were analyzed by cryo-TEM and nanoparticle tracking analysis (NTA), which tracks the Brownian motion of particles to obtain the size range of particles as well as their concentration at various size ranges (Dragovic et al., 2011; Soo et al., 2012) (Fig. 4A). NTA is useful because it overcomes sampling limitations of imaging techniques, especially for samples with low vesicle concentrations due to dilution in the sample preparation (Kim et al., 2019). NTA offers EV quantification on a more feasible time scale as well as desirable sampling.

MCF10A control cells shed a low number of EVs (Fig. 4A), consistent with literature reports that non-tumorigenic/parental cells do not shed EVs in high proportions as compared to malignant cell types (D'Souza-Schorey and Clancy, 2012). In contrast, HAS3 cells released approximately twice as many vesicles as MCF10A cells (Shurer et al., 2019) (Fig. 4A).

The high number of EVs released from HAS cells motivated us to further characterize their microstructure and size distribution by direct imaging using cryo-TEM. For direct comparison with the NTA data, we recovered vesicles post-NTA for imaging (*see* Materials and Methods). Cryo-TEM revealed that the EVs from HAS3 cells were heterogeneous in both shape and diameter (Fig. 4B-D). Interestingly, vesicles historically designated as MVs based on their size of 200 nm-1 μm, contained surface structure while exosomes (50-100 nm) did not (Fig. 4B-D). We believe that this difference in surface structure can be attributed to the differences in the biogenesis pathways of exosomes and MVs. Specifically, MVs adopt their parental cell's glycocalyx while shedding from the cell's plasma membrane (Shurer et al., 2019), while exosomes, which are endosomally trafficked and secreted from the cell through exocytosis, may have different surface structure.

Information about the vesicle surface structure provided by cryo-TEM can be used in conjunction with particle size measurements to differentiate between subpopulations of EVs. Because the native structure remains unaltered, we expect cryo-TEM to provide an accurate analysis of vesicle diameters, which can be used for comparison with NTA data. Therefore, EVs were recovered following NTA and subsequently plunge-frozen for imaging and analysis by cryo-TEM. The particle size distributions of EVs from HAS3 cells collected by NTA and cryo-TEM both reached their maxima at comparable vesicle sizes (Fig. 5A, B and Fig. S2). There were distinct differences, however, between the size distributions measured by these two complementary techniques. Data from the NTA tracked particles range from 20-1000 nm in diameter with its maximum around 50 nm (Fig. 5A). The distribution of vesicles identified with cryo-TEM was broader, ranging from 20-1275 nm in diameter. The strongest peak in the cryo-TEM distribution was around 75 nm and larger MVs comprised a

great proportion of vesicles compared to the NTA data, resulting in a broader tail in the size distribution (Fig. 5B). Vesicles less than 100 nm accounted for 42% of all vesicles tracked by NTA, but only 26% of vesicles detected with cryo-TEM.

The NTA size distribution is artificially truncated due to the sensitivity of detectable diameter range of the instrument. The upper range of accurately detectable particles is ~1000 nm, and particles larger than this are usually excluded from analysis. Brownian motion limits the maximum size of detectable particles. As vesicles become too large, their Brownian motion becomes difficult to track over reasonable acquisition times, therefore the software either fails to detect these particles or measures them with high inaccuracy (Yang et al, 2014). Cryo-TEM in comparison does not exclude vesicles with larger diameters but confirms that the proportion of HAS3 vesicles greater than 1000 nm is still negligible. For instance, the largest particles tracked by NTA in this study were ~1000 nm in diameter and comprised < 0.1% of all vesicles analyzed. Similarly, vesicles larger than 1000 nm accounted for only 0.5% of all vesicles observed with cryo-TEM. Note, that here we assume that the blotting process prior to plunge-freezing of the sample will affect the total number of vesicles observed, but not their size distribution.

The origin of other discrepancies between the NTA and cryo-TEM data could be attributed to several factors, necessitating the need to complement the techniques when possible. The cryo-TEM size distribution exhibits a lower signal-to-noise ratio due to the low-throughput nature of the technique, which results in lower sample statistics. Despite this limitation, we believe the number of vesicles measured by cryo-TEM (n = 642) in this study was sufficiently high to use as a comparison to NTA data. A larger data set, however, would undoubtedly provide a more refined result. Debris in the cell media likely influenced the distribution of particle diameters in the NTA data. Post-NTA cell media examined with cryo-TEM showed the presence of a large amount of debris of varying sizes (Fig. S3, B). NTA tracks any material that diffuses and has a refractive index (Filipe et al., 2010). The software also assumes that the particles are spherical and derives a hydrodynamic diameter for both vesicular and non-vesicular material. This analysis means that, in NTA, it is difficult to reliably differentiate between vesicles and debris within a solution, and the diameters of any particle that moves within the solution is recorded. This lack of discrimination between populations could explain the difference in the relative proportions of smaller to larger vesicles in the NTA and cryo-TEM data. Superficially, most of the post-NTA debris appeared larger than the sizes of exosomes but appeared to contain aggregates of smaller structures that were about the size of exosomes (Fig. S3). It is not clear, but we hypothesize that these structures could have aggregated after NTA and before vitrification. While low in sample statistics, the main advantage of direct imaging by cryo-TEM is the ability to resolve vesicle surface structure (Fig. 4B-D), which provides a route to identify the microvesicle subpopulation as discussed above. Compared to the typical cutoff of 200 nm used to separate the particle counts from NTA into microvesicles and exosomes, we found that for HAS3-overexpressing MCF10A cells vesicles as small as 90 nm exhibited distinct surface features in cryo-TEM, which we conclude as a signature to identify microvesicles. By imaging all vesicles in the range of 80-120 nm at high resolution, we separated the size distribution into the microvesicle and exosome population as shown in Fig. 5C based on surface structure.

Conclusions

This study compared the use of confocal fluorescence microscopy and both conventional and cryo-SEM in order to evaluate cell morphology and structures dimensionally consistent with MVs on membrane protrusions in cells. Additionally, we used NTA and cryo-TEM to compare the size distributions from each technique and validate the presence and structure of EVs from sample suspensions. Our results highlight that there is no specific workhorse technology that can provide a comprehensive analysis of cell morphology and EV presence and morphology. The limitations of one technique, however, can be compensated by the merits of the respective additional techniques that we explored here. Conventional SEM captures 3D tubular projections and spherical structures coming from the plasma membrane, but the cells are desiccated during the sample preparation process, which alters their native state. Cryo-SEM preserves the water content of these cells but can affect the structure of delicate projecting features and cause them to collapse. NTA provides statistics of the distributions of particles in a given suspension, but cryo-TEM can differentiate between vesicles and debris, as well as probe vesicle morphology and surface structure. The choice of whether to use NTA or cryo-TEM to profile EVs depends on the question under examination. NTA is the more suitable technique when one wants to compare the relative concentrations of vesicles that are released from cells of interest. NTA is also useful when high-throughput information of a high concentration of vesicles is desired. Finally, NTA is useful when the majority of the particles are less than 1000 nm in diameter, especially in polydisperse samples. Cryo-TEM is the more useful technique when imaging either very small or very large populations of vesicles, particularly those near the detection range of NTA instruments. Cryo-TEM can visualize surface morphology, making it the method of choice for distinguishing between subpopulations of vesicles. Finally, cryo-TEM is more useful when examining media that is contaminated with other non-vesicular components, such as those that may be produced during the isolation process.

Together, these techniques reveal both the relative size distribution from respective samples and the morphology of isolated vesicles. The combination of glycocalyx engineering and multiple microscopy techniques reported here provide a technical roadmap for differentiating between exosome and microvesicle populations, based upon more detailed data than just size. In-depth characterization of each EV subpopulation is beneficial for better understanding of the roles of each in pathological and physiological states. Overall, our study reaffirms the necessity of a multi-platform approach that can help experimentalists better characterize EV presence, size and morphology, as well as the ability of certain cells to release them in a way that the respective techniques cannot do individually.

Supplementary Material

Refer to Web version on PubMed Central for supplementary material.

Acknowledgements

The authors would like to thank Mick Thomas and John Grazul for microscopy support. We thank Brian Kirby, Siyoung Choi, Michael Zachman and Jennie A.M.R. Kunitake for helpful discussions. This work was supported by the National Institute of Health/National Cancer Institute [Grant U54 CA210184], the Packard Foundation and a

National Science Foundation (NSF) Graduate Research Fellowship (L.M.R.). L.A.E. and C.F. acknowledge support from the Human Frontiers Science Program (RGP0016/2017). This work made use of the Cornell Center for Materials Research Shared Facilities which are supported through the NSF MRSEC program [DMR-1719875]. The FEI Titan Themis 300 was acquired through NSF-MRI-1429155, with additional support from Cornell University, the Weill Institute and the Kavli Institute at Cornell. Cornell Nanoscale Science and Technology Facility supported through the NSF Grant (ECCS-1542081), Biotechnology Resource Center (BRC) Imaging Facility [NIH S10OD018516].

REFERENCES

Antonyak MA, Li B, Boroughs LK, Johnson JL, Druso JE, Bryant KL, Holowka DA, Cerione RA, 2011 Cancer cell-derived microvesicles induce transformation by transferring tissue transglutaminase and fibronectin to recipient cells. Proc. Natl. Acad. Sci 108, 4852–4857. 10.1073/pnas.1017667108 [PubMed: 21368175]

Becker A, Thakur BK, Weiss JM, Kim HS, Peinado H, Lyden D, 2016 Extracellular Vesicles in Cancer: Cell-to-Cell Mediators of Metastasis. Cancer Cell 30, 836–848. 10.1016/J.CCELL.2016.10.009 [PubMed: 27960084]

Charuvi D, Nevo R, Kaplan-Ashiri I, Shimoni E, Reich Z, 2016 Studying the Supramolecular Organization of Photosynthetic Membranes within Freeze-fractured Leaf Tissues by Cryo-scanning Electron Microscopy. J. Vis. Exp 112, e54066 10.3791/54066

Cheng XB, Sato N, Kohi S, Yamaguchi K, 2013 Prognostic impact of hyaluronan and its regulators in pancreatic ductal adenocarcinoma. PLoS ONE 8, e80765 10.1371/journal.pone.0080765 [PubMed: 24244714]

Cochard H, Bodet C, Améglio T, Cruiziat P, 2000 Cryo-scanning electron microscopy observations of vessel content during transpiration in walnut petioles. Facts or artifacts? Plant Physiol. 124, 1191–202. 10.1104/PP.124.3.1191 [PubMed: 11080296]

Colombo M, Raposo G, Thery C, 2014 Biogenesis, secretion, and intercellular interactions of exosomes and other extracellular vesicles. Annu. Rev. Cell Dev. Biol 30, 255–289. [PubMed: 25288114]

Desrochers LM, Bordeleau F, Reinhart-King CA, Cerione RA, Antonyak MA, 2016 Microvesicles provide a mechanism for intercellular communication by embryonic stem cells during embryo implantation. Nat. Commun 7, 11958 10.1038/ncomms11958 [PubMed: 27302045]

Dragovic RA, Gardiner C, Brooks AS, Tannetta DS, Ferguson DJP, Hole P, Carr B, Redman CWG, Harris AL, Dobson PJ, Harrison P, Sargent IL, 2011 Sizing and phenotyping of cellular vesicles using Nanoparticle Tracking Analysis. Nanomedicine Nanotechnol. Biol. Med 7, 780–788. 10.1016/j.nano.2011.04.003

D'Souza-Schorey C, Clancy JW, 2012 Tumor-derived microvesicles: shedding light on novel microenvironment modulators and prospective cancer biomarkers. Genes Dev. 26, 1287–99. 10.1101/gad.192351.112 [PubMed: 22713869]

Dubochet J, McDowall AW, 1981 Vitrification of pure water for electron microscopy. J. Microsc. 124, 3–4. 10.1111/j.1365-2818.1981.tb02483.x

Echlin P, Paden R, Dronzek B, Wayte R, 1970 Scanning electron microscopy of labile biological material maintained under controlled conditions. in Scanning Electron Microscopy/1970, Proceedings of the Third Annual Scanning Electron Microscope Symposium, Johari O (ed.), IIT Research Institute, Chicago, Illinois, 1970, p. 49–56

Echlin P, 1971 The examination of biological material at low temperatures, in Scanning Electron Microscopy/1971 (Part I), Proceedings of the Fourth Annual Scanning Electron Microscope Symposium, 1971, p. 225–232

Feng Q, Zhang C, Lum D, Druso JE, Blank B, Wilson KF, Welm A, Antonyak MA, Cerione RA, 2017 A class of extracellular vesicles from breast cancer cells activates VEGF receptors and tumour angiogenesis. Nat. Commun 8, 14450 10.1038/ncomms14450 [PubMed: 28205552]

Furie B, Furie BC, 2004 Role of platelet P-selectin and microparticle PSGL-1 in thrombus formation. Trends Mol. Med 10, 171–178. 10.1016/J.MOLMED.2004.02.008 [PubMed: 15059608]

Goldstein JI, Newbury DE, Michael JR, Ritchie NWM, Scott JHJ, Joy DC, 2018 Scanning Electron Microscopy and X-Ray Microanalysis, 4th edn. Springer, New York.

György B, Szabó TG, Pásztói M, Pál Z, Misják P, Aradi B, László V, Pállinger É, Pap E, Kittel Á, Nagy G, Falus A, Buzás EI, 2011 Membrane vesicles, current state-of-the-art: Emerging role of extracellular vesicles. Cell. Mol. Life Sci 68, 2667 10.1007/s00018-011-0689-3 [PubMed: 21560073]

Issman L, Brenner B, Talmon Y, Aharon A, 2013 Cryogenic transmission electron microscopy nanostructural study of shed microparticles. PLoS ONE 8, e83680 10.1371/journal.pone.0083680 [PubMed: 24386253]

Joy DC, Joy C, 1995 Dynamic Charging in the Low Voltage SEM. JMSA 1, 109–112.

Kim A, Ng WB, Bernt W, Cho NJ, 2019 Validation of Size Estimation of Nanoparticle Tracking Analysis on Polydisperse Macromolecule Assembly. Sci. Rep 9, 2639 10.1038/s41598-019-38915-x [PubMed: 30804441]

Kim CW, Lee HM, Lee TH, Kang C, Kleinman HK, Gho YS, 2002 Extracellular membrane vesicles from tumor cells promote angiogenesis via sphingomyelin. Cancer Res. 62, 6312–7. [PubMed: 12414662]

Koifman N, Biran I, Aharon A, Brenner B, Talmon Y, 2017 A direct-imaging cryo-EM study of shedding extracellular vesicles from leukemic monocytes. J. Struct. Biol 198, 177–185. 10.1016/j.jsb.2017.02.004 [PubMed: 28254382]

Koistinen V, Kärnä R, Koistinen A, Arjonen A, Tammi M, Rilla K, 2015 Cell protrusions induced by hyaluronan synthase 3 (HAS3) resemble mesothelial microvilli and share cytoskeletal features of filopodia. Exp. Cell Res. 337, 179–191. 10.1016/J.YEXCR.2015.06.016 [PubMed: 26162854]

Kultti A, Rilla K, Tiihonen R, Spicer AP, Tammi RH, Tammi MI, 2006 Hyaluronan synthesis induces microvillus-like cell surface protrusions. J. Biol. Chem. 281, 15821–15828. 10.1074/jbc.M512840200 [PubMed: 16595683]

Le MTN, Hamar P, Guo C, Basar E, Perdigão-Henriques R, Balaj L, Lieberman J, 2014 miR-200–containing extracellular vesicles promote breast cancer cell metastasis. J. Clin. Invest 124, 5109–5128. 10.1172/JCI75695 [PubMed: 25401471]

Liu Y, Zhu X, Zeng C, Wu P, Wang H, Chen Z, Li Q, 2014 Microvesicles secreted from human multiple myeloma cells promote angiogenesis. Acta Pharmacol. Sin 35, 230–238. 10.1038/aps.2013.141 [PubMed: 24374814]

Mahamid J, Aichmayer B, Shimoni E, Ziblat R, Li C, Siegel S, Paris O, Fratzl P, Weiner S, Addadi L, 2010 Mapping amorphous calcium phosphate transformation into crystalline mineral from the cell to the bone in zebrafish fin rays. Proc. Natl. Acad. Sci 107, 6316–6321. 10.1073/pnas.0914218107 [PubMed: 20308589]

McCully ME, Canny MJ, Huang CX, 2009 Cryo-scanning electron microscopy (CSEM) in the advancement of functional plant biology. Morphological and anatomical applications. Funct. Plant Biol 36, 97 10.1071/FP08304

Melo SA, Luecke LB, Kahlert C, Fernandez AF, Gammon ST, Kaye J, LeBleu VS, Mittendorf EA, Weitz J, Rahbari N, Reissfelder C, Pilarsky C, Fraga MF, Piwnica-Worms D, Kalluri R, 2015 Glypican-1 identifies cancer exosomes and detects early pancreatic cancer. Nature 523, 177–182. 10.1038/nature14581 [PubMed: 26106858]

Menck K, Scharf C, Bleckmann A, Dyck L, Rost U, Wenzel D, Dhople VM, Siam L, Pukrop T, Binder C, Klemm F, 2015 Tumor-derived microvesicles mediate human breast cancer invasion through differentially glycosylated EMMPRIN. J. Mol. Cell Biol 7, 143–153. 10.1093/jmcb/mju047 [PubMed: 25503107]

Moeck L, Pedram K, Roy AR, Krishnan V, Gustavsson A-K, Dorigo O, Bertozzi CR, Moerner WE, 2019 Quantitative Super-Resolution Microscopy of the Mammalian Glycocalyx. Dev. Cell 50, 57–72. 10.1016/j.devcel.2019.04.035 [PubMed: 31105009]

Muralidharan-Chari V, Clancy JW, Plou C, Romao M, Chavrier P, Raposo G, D'Souza-Schorey C, Sedgwick A, D'Souza-Schorey C, 2010 Microvesicles: mediators of extracellular communication during cancer progression. J. Cell Sci 123, 1603–1611. 10.1242/jcs.064386 [PubMed: 20445011]

Nakamura Y, Miyaki S, Ishitobi H, Matsuyama S, Nakasa T, Kamei N, Akimoto T, Higashi Y, Ochi M, 2015 Mesenchymal-stem-cell-derived exosomes accelerate skeletal muscle regeneration. FEBS Lett. 589, 1257–1265. 10.1016/j.febslet.2015.03.031 [PubMed: 25862500]

Pokharel D, Padula MP, Lu JF, Tacchi JL, Luk F, Djordjevic SP, Bebawy M, 2014 Proteome analysis of multidrug-resistant, breast cancer derived microparticles. J. Extracellullar Vesicles 3, 24384 10.3402/jev.v3.24384

Rilla K, Pasonen-Seppänen S, Deen AJ, Koistinen VVT, Wojciechowski S, Oikari S, Kärnä R, Bart G, Törrönen K, Tammi RH, Tammi MI, 2013 Hyaluronan production enhances shedding of plasma membrane-derived microvesicles. Exp. Cell Res 319, 2006–2018. 10.1016/j.yexcr.2013.05.021 [PubMed: 23732660]

Shurer CR, Kuo JC-H, Roberts LM, Gandhi JG, Colville MJ, Enoki TA, Pan H, Su J, Noble JM, Hollander MJ, O'Donnell JP, Yin R, Pedram K, Möckl L, Kourkoutis LF, Moerner WE, Bertozzi CR, Feigenson GW, Reesink HL, Paszek MJ, 2019 Physical Principles of Membrane Shape Regulation by the Glycocalyx. Cell 177, 1757–1770. 10.1016/j.cell.2019.04.017 [PubMed: 31056282]

Soo CY, Song Y, Zheng Y, Campbell EC, Riches AC, Gunn-Moore F, Powis SJ, 2012 Nanoparticle tracking analysis monitors microvesicle and exosome secretion from immune cells. Immunology 136, 192–197. 10.1111/j.1365-2567.2012.03569.x [PubMed: 22348503]

Soule HD, Maloney TM, Wolman SR, Peterson WD, Brenz R, McGrath CM, Russo J, Pauley RJ, Jones RF, Brooks SC, 1990 Isolation and characterization of a spontaneously immortalized human breast epithelial cell line, MCF-10. Cancer Res. 50, 6075–86. [PubMed: 1975513]

Szatanek R, Baj-Krzyworzeka M, Zimoch J, Lekka M, Siedlar M, Baran J, 2017 The Methods of Choice for Extracellular Vesicles (EVs) Characterization. Int. J. Mol. Sci 18(6), 1153 10.3390/ijms18061153

Tannetta D, Dragovic R, Alyahyaei Z, Southcombe J, 2014 Extracellular vesicles and reproduction-promotion of successful pregnancy. Cell. Mol. Immunol 11, 548–563. 10.1038/cmi.2014.42 [PubMed: 24954226]

Utsumi Y, Sano Y, Fujikawa S, Funada R, Ohtani J, 1998 Visualization of cavitated vessels in winter and refilled vessels in spring in diffuse-porous trees by cryo-scanning electron microscopy. Plant Physiol. 117, 1463–71. [PubMed: 9701601]

van der Pol E, Böing AN, Harrison P, Sturk A, Nieuwland R, 2012 Classification, functions, and clinical relevance of extracellular vesicles. Pharmacol. Rev 64, 676–705. 10.1124/pr.112.005983 [PubMed: 22722893]

van Niel G, D'Angelo G, Raposo G, 2018 Shedding light on the cell biology of extracellular vesicles. Nat. Rev. Mol. Cell Biol 19, 213–228. 10.1038/nrm.2017.125 [PubMed: 29339798]

Xu R, Rai A, Chen M, Suwakulsiri W, Greening DW, Simpson RJ, 2018 Extracellular vesicles in cancer — implications for future improvements in cancer care. Nat. Rev. Clin. Oncol 15, 617–638. 10.1038/s41571-018-0036-9 [PubMed: 29795272]

Yuana Y, Sturk A, Nieuwland R, 2013 Extracellular vesicles in physiological and pathological conditions. Blood Rev. 27, 31–39. 10.1016/j.blre.2012.12.002 [PubMed: 23261067]

Highlights

- Characterization of extracellular vesicle (EV) release from human breast cell lines
- SEM shows vesicular structures budding off of membrane tubes driven by HAS3
- Cryo-TEM reveals two EV sub-populations based upon size and structural detail
- EV surface structure is identified as biomarker for MVs compared to exosomes

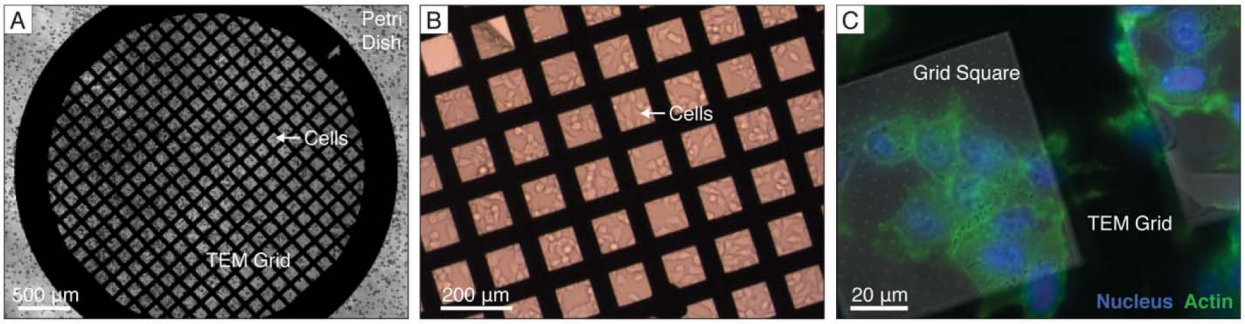

Fig. 1. On-grid cell culture set up and confocal imaging for on-grid validation.

(A) Bright-field image of MDA-MB231 cells seeded on a fibronectin-functionalized carbon-coated gold TEM grid in a cell culture dish (arrow represents location of cells on the suspended fibronectin-coated carbon support film). **(B)** Bright-field image and **(C)** fluorescence confocal image of MDA-MB231 cells grown uniformly on the grid, including in the electron-transparent grid squares. Blue – DAPI (nuclei), green-Phalloidin Alexa Fluor 488 (F-actin).

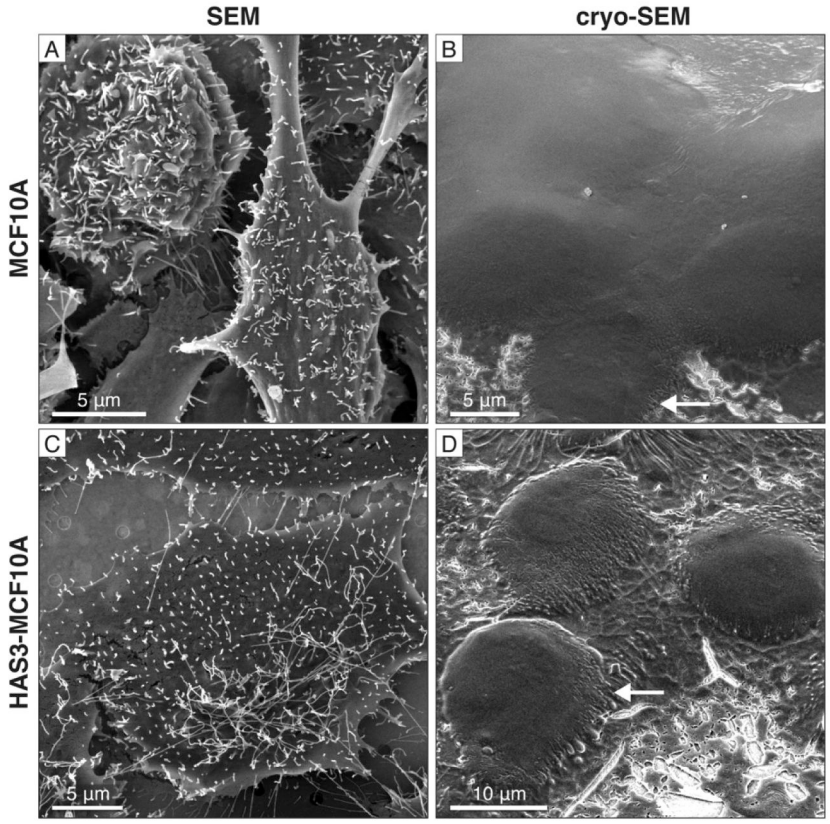

Fig. 2. Cell morphology of HAS3 and MCF10A control cells imaged by conventional and cryo-SEM.

(A) Conventional SEM image of chemically-fixed MCF10A cells. **(B)** Cryo-SEM image of frozen-hydrated MCF10A cells. Tubular extensions are observed (arrow). **(C)** HAS3 cells prepared for conventional SEM with longer tubular extensions compared to the MCF10A controls. **(D)** HAS3 cells imaged by cryo-SEM also show tubular extensions (arrow), but they appear flattened. See Fig. S1 for additional cryo-SEM images of HAS3 cells.

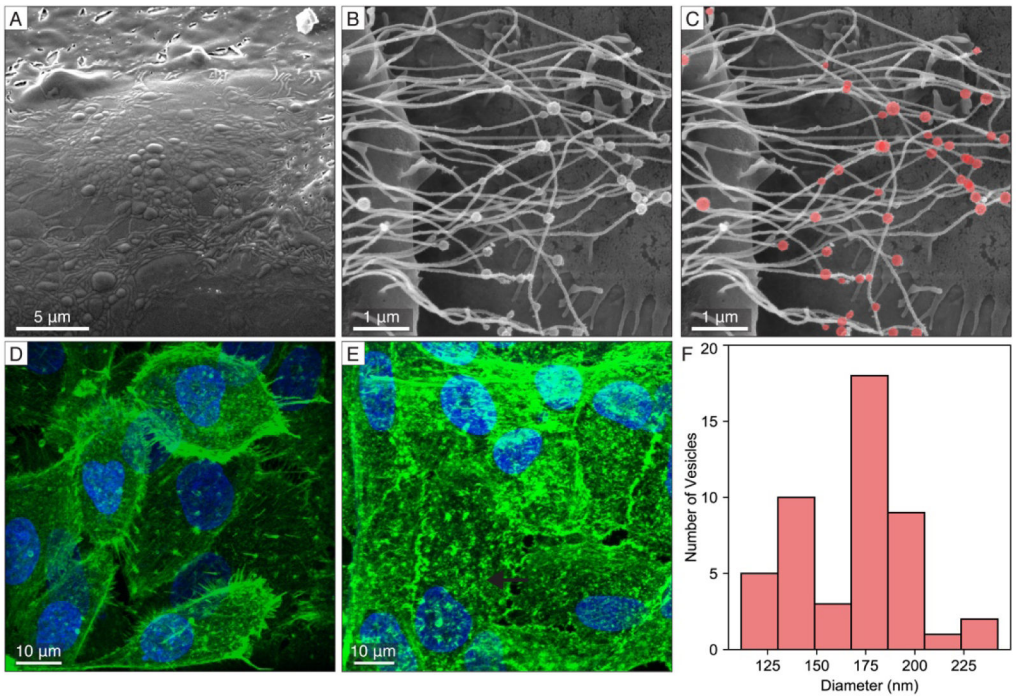

Fig. 3. Cell membrane protrusions and vesicular structures imaged by complementary techniques.

(A) Cryo-SEM of microstructure on the cell membrane of MCF10A control cells. **(B)** Conventional SEM image of tubular extensions from HAS3 cells containing spherical structures along their lengths as highlighted in **(C)**. **(D-E)** Confocal fluorescence microscopy shows a high intensity of actin staining in HAS3 cells **(E)** relative to the MCF10A controls **(D)**, consistent with the presence of numerous long tubular extensions in HAS3 cells. **(F)** Diameter distribution of vesicular structures along the length of membrane extensions from HAS3 cells with most vesicles being dimensionally consistent with microvesicles.

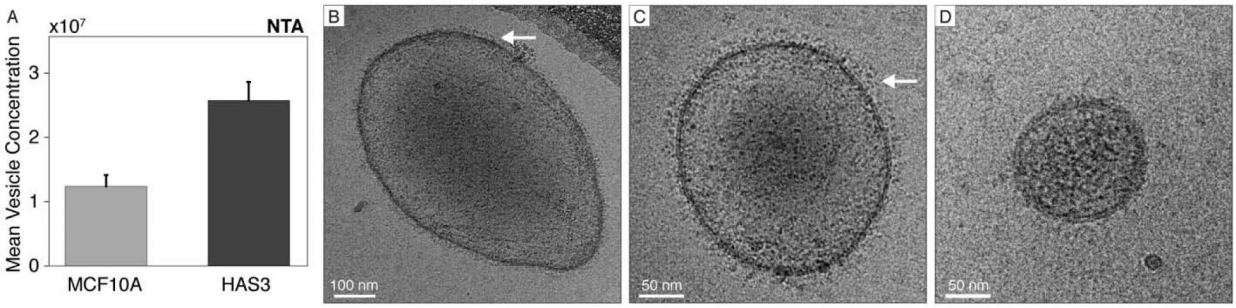

Fig. 4. Extracellular vesicle post-isolation concentration and morphology.

(A) Mean overall particle concentration from nanoparticle tracking analysis (NTA) of EVs shed and/or secreted from MCF10A HAS3 and control cells. Error bars represent standard error of the mean from three individual measurements for each cell line. **(B-D)** Cryo-TEM of frozen-hydrated vesicles post-isolation from HAS3 cells shows heterogeneity in vesicle shape and size. Additionally, larger HAS3 vesicles have prominent surface structure (B-C, arrows), while smaller vesicles have either less or no such surface structure (D).

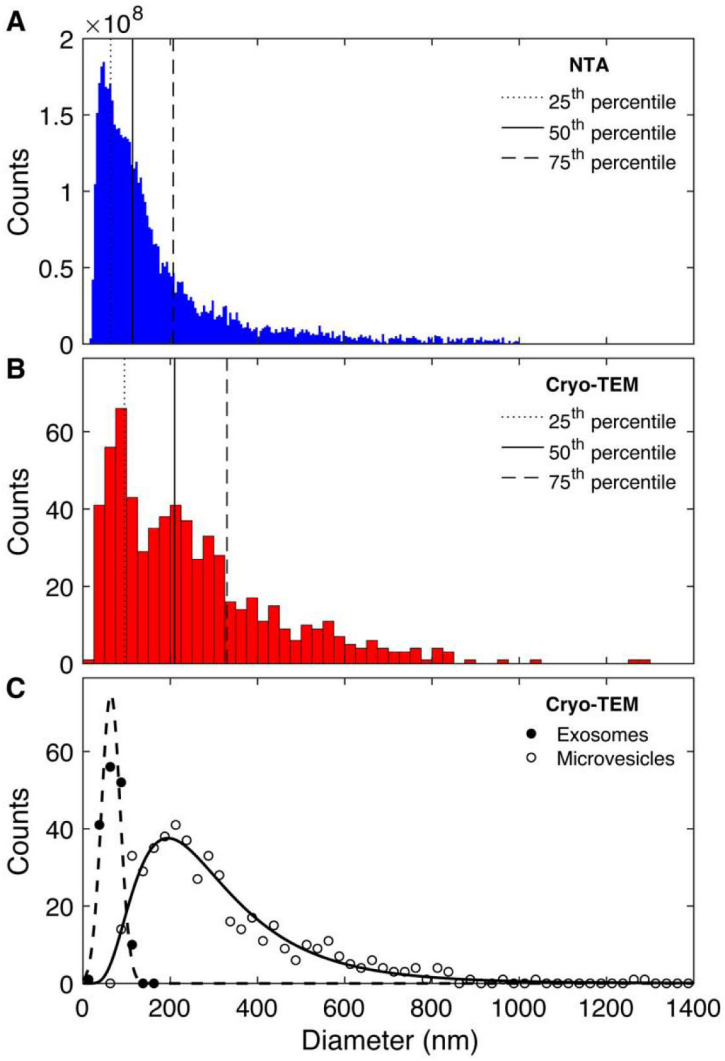

Fig. 5. HAS3 vesicle size distribution measured by NTA and cryo-TEM.

The size distribution of vesicles tracked with **(A)** NTA is significantly different than the distribution of vesicles observed with cryo-TEM **(B)**. Most notably, larger vesicles comprise a greater proportion of vesicles captured by cryo-TEM than NTA. The lower throughput of cryo-TEM is reflected in the smaller number of vesicles measured (n=642). **(C)** Direct cryo-TEM imaging of the vesicle surface structure allows identification of two vesicle subpopulations where those with clear surface features are grouped as Microvesicles while others are labelled Exosomes. Data in (A) and (B) are replotted using the same bin size in Figure S2.